Predicting Intraocular Pressure Utilizing a Highly Nonlinear Solitary Wave (HNSW) Transducer

by

Madison Hodgson

Biomedical Engineering, University of Wisconsin-Madison, 2021

Submitted to the Graduate Faculty of the

Swanson School of Engineering in partial fulfillment

of the requirements for the degree of

Master of Science in Electrical and Computer Engineering

University of Pittsburgh

2023

UNIVERSITY OF PITTSBURGH

SWANSON SCHOOL OF ENGINEERING

This thesis was presented

by

Madison Hodgson

It was defended on

April 7, 2023

and approved by

Dr. Alan George, Professor and Department Chair, Electrical and Computer Engineering

Dr. Murat Akcakaya, Associate Professor, Electrical and Computer Engineering

Thesis Advisors: Dr. Samuel J. Dickerson, Associate Professor, Electrical and Computer
Engineering
and
Dr. Piervincenzo Rizzo, Professor, Civil and Environmental Engineering

Predicting Properties of a Material Utilizing a Highly Nonlinear Solitary Wave (HNSW) Transducer

Madison Hodgson, MS

University of Pittsburgh, 2023

The use of highly nonlinear solitary waves (HNSWs) to nondestructively evaluate materials has recently emerged as a promising method with several key advantages over conventional stress wave-based inspection technologies. The technique is based on the actuation and detection of solitary waves which propagate along an array of spheres (arranged much like a Newton's cradle) and bounce off the specimen to be inspected. HNSW measurement devices require an array of spheres, an electromagnet, and a sensor. This assembly can be called a HNSW transducer. For this thesis, a portable, low-power, wireless transducer was designed, assembled, and tested. The novel transducer design of this work allows HNSW measurements to be taken without wired connections or bulky electronic test equipment and in settings not previously possible. The reliability of the device's measurements was determined by carrying out comparative tests whereby a conventional HNSW transducer and the novel design of this work were used to evaluate a variety of hard and soft materials. The first set of experiments characterized 45 measurements of both steel and low-density Sawbones. The results of the experiments show that the instrument can accurately operate without the support of electronic equipment and with enough accuracy to be useful in real-world settings. In addition to the hard materials, HNSWs were collected from PDMS, and goat corneas to mimic evaluation of the human eye. The PDMS and cornea samples pressurized from 10mmHg to 30mmHg at 5mmHg increments, simulating intraocular pressure (IOP) variations that occur normally in the eye. The data was analyzed using a variety of machine learning algorithms and features to automatically extract IOP values from

HSNW signals captured by the device were determined. The results show that the device can successfully distinguish clinically relevant IOP levels in eyes.

Table of Contents

List of Tables

List of Figures

Preface

The work presented in this thesis is supported by the NSF (Smart and Connected Health program under the National Science Foundation) grant number 2014389.

1.0 Introduction

Non-destructive evaluation (NDE) is the testing of a structure's properties to detect damage or to characterize mechanical or geometric properties. One of the most novel NDE techniques is based around the usage of highly nonlinear solitary waves (HNSWs) which are mechanical stress waves that can travel through a one-dimensional array of spheres in hertzian contact (Figure 1).
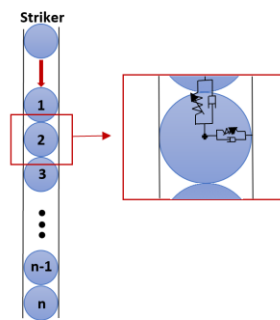
Figure 1 Particles of a one-dimensional array stacked in jerzian contact.

An unexplored application for HNSWs is their use in biomedical applications. If these waves can sense differences in biological materials, it could be applied in ophthalmology to determine damage in an eye to help diagnose and manage diseases such as glaucoma. One major challenge in this application is that previous HNSW transducers are too large to be used with a soft material for the eye. Figure 2 demonstrates the difference between previously used particles and the current design [1].
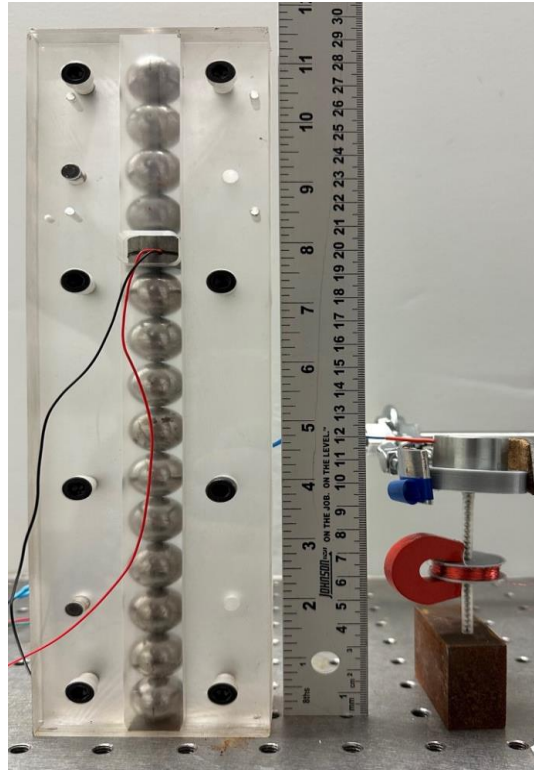
Figure 2 Previously utilized HNSW transdcuer with 19.05mm Ø particles compared to current transducer with 2.38mm Ø particles.

The properties of HNSWs are unique in that the more force contained in the HNSW, the faster the wave moves. This is helpful for specifically identifying the properties of a material where the stiffer the material results in a faster traveling wave. The transducer's one-dimensional array of particles is stacked vertically over the material under inspection where the last particle is in contact with said material. All particles are nonferromagnetic except for two exceptions: the particle that starts the HNSW, the "striker", and the particles involved in measuring the HNSW. The initiation of the HNSW is controlled by the release of the striker particle. After it is picked up with a solenoid, the user controls when the particle is released. Once it contacts the proceeding particle in the chain, the HNSW is formed.

It is possible to track the wave as it travels through the array with a magnetic sensor. The sensor is composed of a coil and permanent magnet positioned around the second grouping of ferromagnetic particles. As the HNSW passes through these particles, it causes a change in the magnetic field which induces a current in the coil and therefore an induced voltage. This voltage is measured, recorded, and stored via a wireless transducer. The exact mechanics of the HNSW and design of the transducer are discussed in more detail later in this paper.

One important aspect of the proposed wireless transducer is that it needs to produce the same results as the previously used wired systems to measure HNSWs, such as an oscilloscope. To test the functionality of the transducer, the HNSW produced by wireless and wired measurements will be compared side-by-side. One feature explored in depth is the time of flight (ToF) defined as the time between when the wave passes through the magnetic sensor after its initiation to when the wave passes back through the sensor after reflecting off the material under inspection. Using steel and low-density Sawbones, referred to as Sawbones for the rest of the paper, the average and standard deviation of the signals produced by the transducer and oscilloscope can be compared with a t-test.

Once it is verified that the transducer can produce comparable results, the next step is utilizing the ToF and other features to gauge if a miniaturized transducer is sensitive enough to detect changes in the HNSW. Comparing the ToFs in steel, Sawbones, PDMS provide a large enough range to test if the transducer works in previously characterized materials as well as biologically similar materials.

The transducer can be used to identify the material under inspection and different properties in the same material. One example is the classification of pressurized polydimethylsiloxane (PDMS) membranes. Further evaluating HNSWs, a medium tree, linear SVM, subspace

3

discriminant, a narrow neural network, and convolutional neural network (CNN) machine learning algorithms can determine if the features manually extracted, the raw signal, or a spectrogram of the HNSW is the most accurate in classifying the material or pressure. The two classification tests are as follows: (1) steel, Sawbones, PDMS at 20mmHg, (2) PDMS at 10mmHg, 15mmHg, 20mmHg, 25mmHg, 30mmHg. Lastly, HNSWs sampled from a goat cornea at the same pressures as PDMS will be evaluated by the best performing algorithms.

1.1 Statement of Work

The scientific discoveries that will be explored in this paper are as follows:

1. Can a wireless transducer function the same as a fully connected way of sampling?

2. Are there noticeable feature differences when looking at one material to the next?

3. What is the best way of representing a HNSW signal that will lead to accurate assessments of the material?

4. In conjunction with 3, what machine learning algorithm is best suited for the classification of materials?

1.2 Research Contributions

In this research, a wireless transducer with full capabilities at collecting HNSWs will allow for remote material testing throughout all disciplines. The transducer has increased sensitivity

allowing for accurate inspection of a HNSW due to its decrease in size making it the smallest HNSW transducer created. From the collected HNSWs, there are several features identified which are considered "new" in the NDE field for HNSWs. One of these features is the duration of oscillation of a solitary wave. The culmination of all identified differences between HNSWs does identify that there is change between the resulting wave and material. Completely new to HNSWs, utilizing a spectrogram for the representation of HNSWs combines the frequency and time domain and proves the most useful in all material identification and looking at differences between the same material. It is used to sense internal pressure changes in an inflated goat cornea, but this method for classifying HNSWs would also be beneficial in damage detection where the damaged and new materials would have different resulting spectrograms. In evaluating new methods for representing HNSWs, this research identifies the current best machine learning classification algorithm for HNSWs produced by soft materials: a convolutional neural network (CNN).

2.0 Background and Motivation

2.1 Intraocular Pressure

The ability to identify and track trends in a patient's IOP is beneficial in gauging overall eye health. The most common issue when monitoring eye health is that a measurement taken once a day struggles to track the fluctuations in IOP that naturally happen in accordance with the circadian rhythm [2]. Additionally, one patient's eyes can have an extensive range of mechanical properties that differ from other patients making it difficult to predict the exact IOP. Consequently, it is more beneficial to track how IOP changes throughout the day rather than identifying its exact properties. Aloy et al. demonstrated the predictive capabilities of vibrations, and how they can help predict the mechanical properties of an eye [3].

By performing constant testing of IOP, it can be beneficial for the identification and monitoring of progression in diseases like glaucoma, uveitis, and retinal detachment [4]. To help the projected 4 million people suffering from glaucoma in 2030 in the United States, our focus of this research is on glaucoma patients and their diagnoses [5]. Glaucoma is an eye disease caused by a high IOP which applies pressure on the optic nerve in the back of the eye. With prolonged high pressure, the patient will start to notice vision loss and eventually go blind if the IOP is not brought under control.

A normal IOP reading can be anywhere between 11mmHg to 21mmHg where everyone has a different baseline. The point at which damage occurs in one eye will not necessarily cause

damage to a different eye, so it is important to note that IOPs higher than 17mmHg are generally when ophthalmologists will start to be concerned. With no cure for glaucoma, the best solution is identifying a lower target IOP for management of the disease. There is no steadfast IOP that is "written in stone" for different progressions of the disease as thoroughly discussed in Sihota et al. [6]. Therefore, it is important to have patients checked often to stop further vision loss. One way to do this is to employ SHM found in NDE applications to track the IOP without causing additional structural damage to the eye.

2.2 Highly Nonlinear Solitary Waves

Non-destructive evaluation (NDE) or non-destructive testing (NDT) is periodically testing and analyzing a structure to identify the properties of the material under inspection or to detect damage. Specifically HNSWs have been utilized extensively in civil engineering and aerospace applications including but not limited to axial stress measurement [7], subsurface void detection[8], concrete hydration monitoring [9], adhesive joints assessment [10], internal pressure measurement [11, 12], delamination detection in laminated composites [13, 14, 15, 16], and characterization of rock materials [17,18]. However, in recent years, HNSWs are now being applied in biomedical applications such as bone assessment [19,20,21] and experimental and numerical analysis on polyurethane foam [22].

Several forms of NDE exist, the most popular being ultrasonic, radiographic, visual, eddy-current, and magnetic-particle testing. A newer method, highly nonlinear solitary waves (NHSWs), gained popularity over the last decade and were proposed as a new SHM technique [23 – 30]. Highly nonlinear solitary waves (HNSWs) are compact stress waves that can propagate under special materials arrangements such as a one-dimensional array made of spheres [31-35]. HNSWs are different than waves typically encountered in ultrasound. Those waves are linear and are characterized by having a return force linearly dependent on the displacement. HNSWs are instead characterized by the fact that the return force F is nonlinearly proportional to the displacement from equilibrium according to Hertz's law [33-36] $F=k\delta^{3/2}$. Here δ is the indentation between two adjacent identical interacting beads, k is the stiffness equal to $(E/2R)[3(1−\nu^2)]$ where R, ν and E are the particles' radius, Poisson ratio, and modulus, respectively. Another distinctive feature is that wave amplitude and speed are proportional, i.e., a stronger pulse propagates faster than a weak pulse. An advantage of HNSWs with respect to conventional waves is tunability: a solitary pulse can be tuned by changing the properties and/or the geometry of the grains to attain the desired wavelength, amplitude, and speed. For example, the speed and amplitude of the traveling pulse can be increased by reducing the diameter of the beads.

The technique relies on the dynamic interaction between the HNSWs propagating along the chain and the material to be inspected/monitored, which is in dry point-contact with the last particle of the chain. The key advantage is the simplicity of the overall setup. A solitary wave, hereinafter referred to as the incident solitary wave (ISW), mechanically triggered at one end of the chain propagates through the chain and reaches the opposite end of the array. Here, the ISW reflects giving rise to one or two solitary waves, the primary and the secondary reflected waves

8

(PSW and SSW). Several studies proved that the amplitude and time of flight (ToF) of these reflected pulses depend also on the mechanical and geometric characteristics of the element to be evaluated. Other advantages of the HNSW-based technique with respect to existing NDE methods are related to the specific applications. For example, HNSWs were applied in cementitious materials [37] and compared against the ultrasonic pulse velocity method (UPV). With respect to the latter, it was demonstrated that HNSW-based approach is cost effective, exploits more parameters (ToF, speed, and amplitude of the reflected pulses) instead of the ultrasonic speed alone, and does not require access to any back-wall. Monitoring these waves with a transducer can help sense minute differences in IOP within an eye and can be tested on PDMS, a known material that can replace the vitreous humor in an eye.

2.3 Features of a HNSW

In addition to ToF, which was mentioned in the previous section, there are other features found in a HNSW that can be indicative to what material is under inspection. The primary features include the ToF, ratio between peaks, solitary wave oscillation, and frequency content of a solitary wave. A full list of features with the full name, abbreviation, and description is found in the appendix. Figure 3 contains depictions of the features found in a HNSW which will be discussed further in this section.
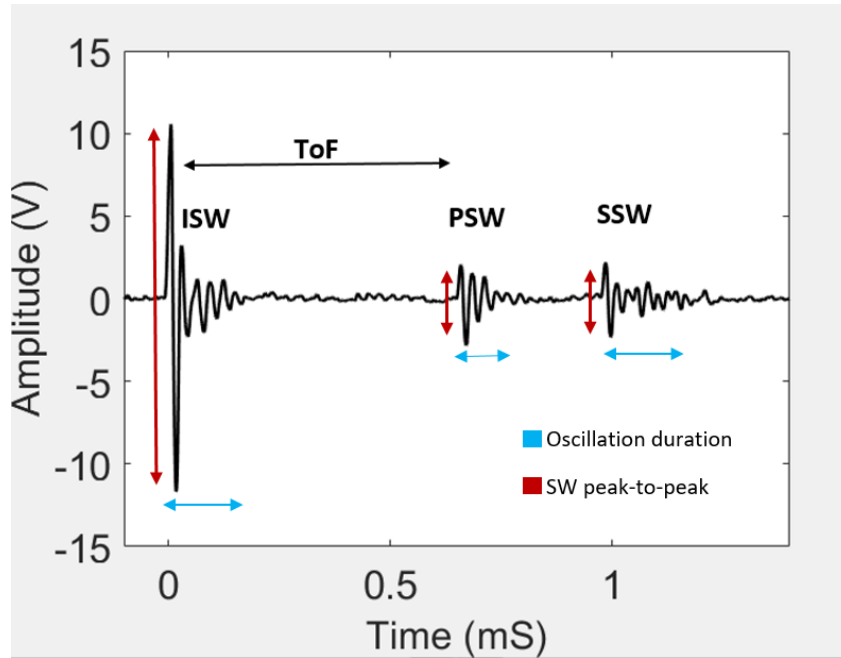
Figure 3 Features, ToF, Oscillation duration, and the ratio of the peak-to-peak are important identifying factors of a HNSW. This wave is taken from PDMS at 10mmHg.

The ToF not only refers to the distance between the start of an ISW and the start of a PSW, but also the time distance between the PSW and SSW (given that the SSW exists). In specific, the start of a solitary wave is identified by a rate of change of ~.26 V/µS after amplification and filtering. This rate was identified through numerous HNSW samples and was found to accurately capture the start of a solitary wave while ignoring noise.

One of the other features previously utilized for material detection is the ratio of the peak-to-peak amplitude of the PSW to the ISW [38]. In addition, the ratio of the SSW to ISW is also used. It is thought that the higher the ratio, the stiffer a material is. When the HNSW reaches the end of the array of particles, stiffer materials absorb less of the energy from the wave and transfer more of the ISW back up to the chain forming the PSW.

Solitary wave oscillation is a new feature observed in HNSWs measured by the duration of oscillation in a SW. There are two reasons why a material would produce a higher oscillation. One is caused by the produced vibrations of the particle after the HNSW reflects off the material under inspection: most common in softer materials. The second reason is due to the combined arrival of the PSW and SSW. The shorter the ToF between the two peaks correlates to an increased stiffness in the material.

Lastly, the frequency content of the ISW, PSW and SSW, offer insight into those vibrations. The peak frequency in Hertz and the magnitude of that frequency response are additional features that may help classify the material under inspection.

2.4 IOP Measuring Techniques

There are many techniques to measure the IOP. The most reliable measurements for IOP are Goldmann applanation tonometry (GAT) seen in Figure 4 [39]. Invented in 1948, this tonometer uses a cone to push on the center of an anaesthetized cornea. By applying force, the cone flattens the top of the cornea and using Fick's law $P = F/S$, where P is pressure, S is surface area, and F is the force, the IOP of an eye can be determined. One of the main drawbacks in this tonometer technique is the invasiveness for the patient who needs to go under localized anesthesia to perform the test. Additionally, the IOP measurement is dependent on other properties of the cornea such as thickness and curvature [40, 41].

Figure 4 Goldmann applanation tonometer used to measure the internal eye pressure. The component highlighted in the red circle is the tip that would come in contact with the cornea.

Given the nature of GAT, a non-contact tonometer was created and named air-puff tonometry. This tonometer uses a puff of air to flatten the cornea and requires no topical anesthetic applied to the patient. However, in a comparative study between GAT and air-puff tonometry, it was found the air-puff tonometer had a much higher standard deviation in its predicted IOP than the applanation tonometer [42].

A hand-held device to measure IOP, the Tono-pen, requires the administrator to touch the end of the pen to the patient's eye. In a study comparing the Tono-pen to the applanation tonometer, the Tono-pen performed similarly to an applanation tonometer but was not able to reproduce results in multiple trials [43]. It was also found that the Tono-pen breaks down in higher

pressures where 100% of scleral measurements at these higher pressures had a high standard deviation [44].

A way to create a better tonometer than the GAT and the Tono-pen would be to perform IOP measurements over the eyelid. This eliminates the need for general anesthesia in GAT and avoids sterilization issues found in corneal contact with the Tono-pen. While air-puff tonometry does not have direct contact with the cornea, it is known to be inaccurate in IOP measurements with the results often giving a range of possible IOP values rather than a single predicted IOP. An ideal device would have the accuracy of the GAT, the non-corneal contact in the air-puff tonometer, and hand held abilities of the Tono-pen

3.0 Device to Measure HNSW

3.1 Transducer Design

A close-up view of our new transducer is presented in Figure 5B. The array is formed by 24 particles, and it is surmounted by a commercial solenoid. The gap between the solenoid and the topmost ball, hereinafter referred to as the striker, is 4 mm. ISWs are generated mechanically by lifting and releasing the striker. The waves are measured with a 10 mm wide coil made of 36 AWG electromagnetic wire using the inverse magnetostrictive effect, which states that a pulse propagating through a ferromagnetic material modulates a strain in the material which in turn modulates an existing magnetic field, which creates current in the coil. The resistance of the coil is 85.4 Ω. The array is housed in a 3D printed frame made of a clear resin [45]. The striker and the four particles wrapped by the coil are made of ferromagnetic materials whereas the remaining particles are made of stainless steel. An example of the time-waveform is presented in Figure 5B.
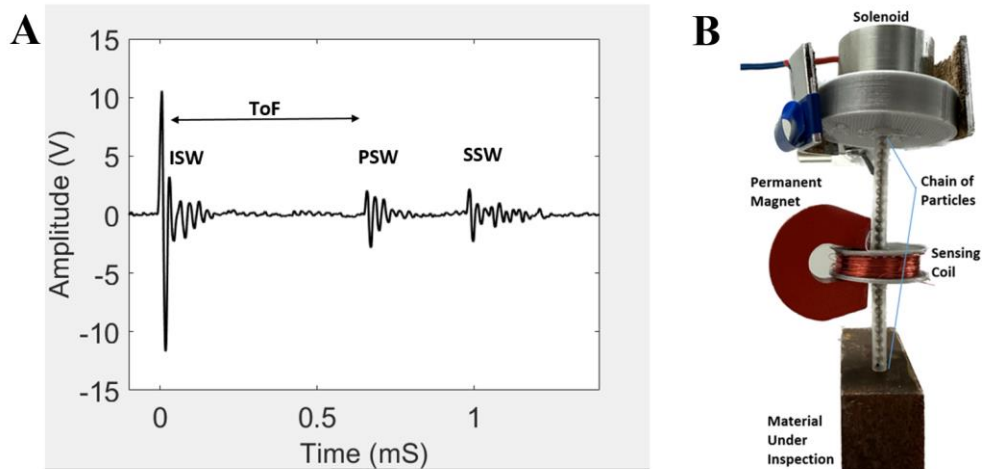
Figure 5 HNSW taken from PDMS inflated to 10mmHg (A) and the HNSW transducer with all labled components (B).

The difference in time between the arrival of the ISW and the PSW represents the ToF. The time waveforms show both positive and negative voltage. When the solitary wave travels through the constant magnetic field induced by the permanent magnet, it increases the compression between two adjacent particles, and it creates a positive gradient of the magnetic flux, which in turn induces the positive voltage. When the pulse moves away, the dynamic compression disappears, a negative gradient of the magnetic flux is induced, and the output voltage has a negative gradient. The integral of the waveforms is proportional to the dynamic contact force between particles [37].

3.2 Circuit Design

3.2.1 Electronic Design

A custom printed circuit board (PCB) was designed and assembled to replace the conventional data acquisition system used in typical wired configurations. Figure 6 shows the block diagram of the circuit and how all the components interact with each other. The size of the PCB is nearly half the first PCB [16] developed by our group. To accomplish high speed data acquisition, the PCB includes a solenoid driver and flyback diode, input operational amplifiers and a low pass filter, an analog to digital converter (ADC), a microcontroller (MCU) and a Bluetooth module.
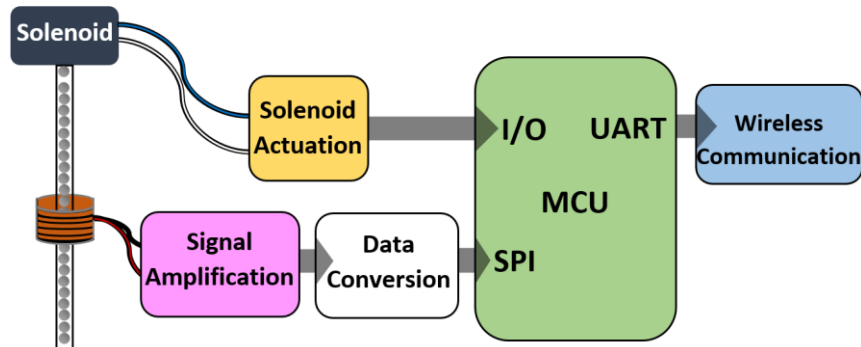
Figure 6 Block diagam of circuit used to control start of the HNSW and store the results.

The MCU is mounted on a Teensy 4.0 breakout board and is the brains of the transducer. This chip has an ARM Cortex-M7 that operates at 600MHz. In addition, the MCU has 512K of usable RAM which is utilized as temporary storage for the incoming HNSW before it is transferred to the output.

The device supports two modes for data transfer. The first is utilizing a 16 MHz UART connection to the Bluetooth module which subsequently streams data to a mobile application. The

second is a serial connection to a laptop that saves data at 480MHz. The serial connection also allows for off-board programming and custom clock frequencies in addition to faster data acquisition.

The microcontroller breakout board is powered by a 3.7V 2000mAh LiPo battery connected when operated wirelessly.

To collect a single HNSW waveform, the MCU must initiate current flow through the solenoid which in turn creates a magnetic field. This field, when strong enough, can lift and drop the striker particle. This action is the catalyst for the HNSW. Next, the MCU collects the incoming signal from the ADC after it passes through two operational amplifiers and a low pass filter. The first amplifier is a differential amplifier whose main purpose is to keep the sensitive coil input isolated and change the output current into a readable voltage. The second amplifier's purpose is for filtering and amplification of the signal. The sampling frequency of the signal is 875 kHz, a frequency capable of capturing signals of 4ms or less with sufficient detail. Finally, the MCU saves the received signal within its own RAM before sending it over UART to the Bluetooth chip where the signal can be collected by an app. A photo of the final assembly is presented in Figure 7.
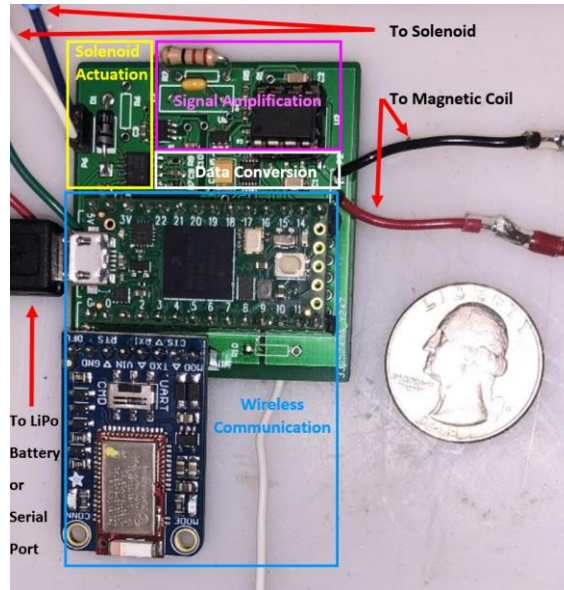
Figure 7 PCB circuit controlling the transducer and HNSW. The solenoid actuation unit is yellow, signal amplification unit is pink, data conversion unit is white, and wireless communication is blue.

3.2.2 Solenoid Actuation and Power Considerations

The power supply requirements are constrained by the amount of current needed to lift and release the striker, and this is proportional to the surface area, the weight of the particle, and the lift-off distance. With the striker particle having a 2.38 mm diameter, it is lighter for the solenoid; however, the decreased surface area works against the electromagnet and makes it more difficult to lift. In this application, the surface area of the particle is the determining step for the power required to lift the striker. After a few trial-and-errors tests, it was determined that a solenoid with ~25 N of suction is sufficient to lift the striker.

Leveraging previous studies [47], the striker is held for 125 mS before being released. The power consumption of the solenoid was evaluated in [48]. During lift and release of the striker, 90mA of current at 10V is consumed by the solenoid. The current is supplied by two 23A 12V

batteries in parallel with each other. They are connected to the PCB by battery holders which allows for the 12V batteries to be replaced as need be much like a household portable device would need to replace its batteries. 12V is chosen due to typical battery degradation during use. In early battery use, there is a 10-15% voltage drop followed by little voltage change until the end of the battery's life. Assuming the higher end of 15%, it assures that there will be at minimum 10.2V available to the solenoid during most the battery's life. In addition, it was found that the total current utilized for one strike is .01125As. Each 12V battery provides 60mAHr which would allow for at a maximum 38,400 strikes (120mAhr * 3600s/hr * 1 impact/.01125A). This is the assumed number of signals that can be collected during the batteries' lifetime which minimizes the cost associated with switching out the batteries.

Using a solenoid driver, it is possible to change the pulse-width modulated (PWM) output to the solenoid via its frequency and duty cycle. A single pulse is sent from the MCU to the driver to produce the output which lasts the pulse's duration. By selecting resistors of 200KΩ and 120KΩ, the PWM has a frequency of 25KHz and duty cycle around 35%. Normally when the driver is in standby mode, meaning no pulse was sent from the microcontroller, the output load is connected to the battery on one side and floating on the other. This prevents any current from entering the solenoid and flyback diode that compose the load. The flyback diode is 1N4001 which can handle up to 50V and 1A. When the pulse is sent, the floating end connects to ground and the current flows through the solenoid portion of the load which causes it to turn on and lifts the striker. The pulse returning to zero induces standby mode and the excess current spike caused by the solenoid turning off loops through the diode and solenoid until it dissipates through heat to the environment. By utilizing the driver, it saves space on the PCB in addition to allowing additional tuning parameters that can be modified in the future to allow for a more power-friendly board.

3.2.3 Signal Amplification and Filtering

To visualize the signal, two operational amplifiers (op amps) work in conjunction. One is an isolated differential op amp that works by comparing the voltage difference at both input terminals and creating an amplified version of that difference and its inversion. The input voltage needs to be between ±250 mV. The isolated op amp is powered by 3.3V from the MCU which centers both outputs at 1.29V. Using an isolated op amp is a deliberate choice that stems from the amplitude of the original HNSW before it enters the circuit. The peak-to-peak of the ISW is only a maximum of 120 mV. The isolated op amp has the benefit of a built-in gain of 8.

The two output signals from the isolated op amp need to be summed. This is accomplished with the second op amp with full rail-to-rail output capability. By utilizing a differential topology and choosing resistors of 1 KΩ and 510 kΩ, it is possible to achieve an additional gain of ~1.96. Next, to prevent the summed signals from having negative voltages, a DC offset is employed to center the signal around 1.8V. This offset is formed from voltage regulator which regulates 3.3V from the MCU to 1.8V. The final signal is then between .8V and 2.8V which safety leaves enough of a buffer on both ends.

The frequency of the Incident, Primary, and Secondary waves is present before 80KHz with peaks at or less than 40KHz seen in Figure 8. This trend in frequency content is the same throughout all material analyzed with this transducer. To help filter out excess noise, an 80 kHz low pass filter is the final bridge before the signal can be sent to the ADC.
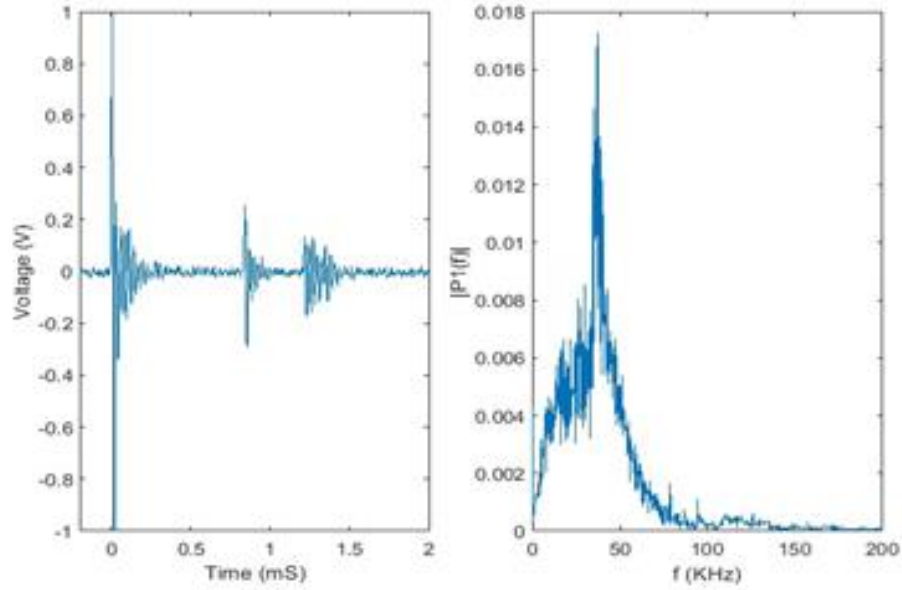
Figure 8 HNSW taken from PDMS and its cooresponding FFT. The peak frequency is seen around 40KHz.

3.2.4 Data Conversion

Passing through the final preprocessing stage, the signal now enters the ADC to be converted into a 16-bit number with a resolution of 65,536. The ADC has a compatible 16-bit resolution and 1Msps sampling rate. The internal components that create the digital output are powered by 3.3V provided by the MCU whereas the analog circuitry is powered by 1.8V which is provided by the same voltage regulator in the operation amplifier circuit.

The ADC is controlled by the MCU through SPI communication. Shortly after the command is given to end the pulse to the solenoid driver, the MCU begins communicating with the ADC. Pulling the conversion start line (equivalent to chip select) high tells the ADC to sample

21

the input signal. After a minimum of 700 nS, the MCU pulls the start line low signaling the ADC to send the bit value of the input signal at that time through its serial data out (SDO). Sending the data to the MCU takes a minimum of 250 nS. Pulling the conversion line high starts this cycle over until sufficient samples have been collected. The ADC is current cautious with standby and data conversion mode only using a maximum of 0.8uA and 1.6 mA, respectively.

Once the striker is lifted and released, the striker takes a variable amount of time to drop and start the HNSW. To avoid any hardcoding of this variable, the code utilizes a buffer within the RAM. The buffer is 200 samples long (N to N + 199) which equates to 400 bytes in RAM storage. Additionally, there is an option to change the length of the signal to be collected. This, much like the buffer, is assigned a location in the RAM of 2 bytes * size of the sample. To populate their buffer in Figure 9, the first sample is taken and placed at the N sample location in the RAM which has a size of 2 bytes to store the entirety of the 16-bit data point. Before moving onto the next sample, the MCU checks whether this sample's voltage is above a threshold of 2.4V. The threshold checks to see when the Incident wave begins by looking for the start of any wave that has a peak of at least 40mV (40mV * 8V/V * 1.96V/V + 1.8V = 2.42V). If the point is below the threshold, the ADC takes another sample, and it is stored in the next location N + 1. This continues until it reaches N + 199. Once a sample is assigned to this last storage location, the cycle restarts and the next point is placed back in data location N, overriding the previous sample that resided there. Once there is a sample above 2.4V, the MCU moves onto the next part of data collection.
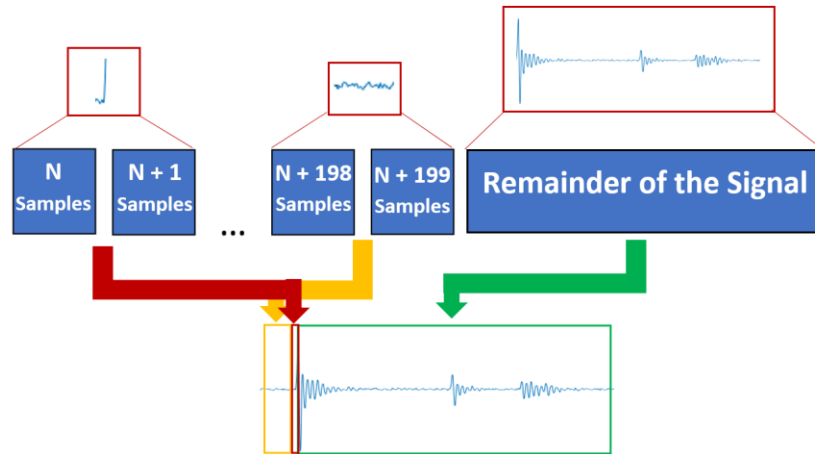
Figure 9 Schematics of the process used to digitize and store the waveforms.

The ADC continually takes samples until it reaches the predetermined sample size. The MCU stores each of these new samples in a secondary RAM location. Once the entire signal is saved in RAM, it is exported through the serial port or over Bluetooth. This is accomplished by finding the sample in the buffer where the threshold was crossed: let us refer to it as "P". Sample P + 1 to Sample N + 199 is the beginning of the signal, preceding Sample N to Sample P. The final signal is created by combining these two buffer segments and the remainder of the data. Doing data collection this way minimizes the RAM taken up through sampling as well as assures the Incident wave is lined up in every HSNW collected.

3.2.5 Wireless Communication

Bluetooth communication is commonplace among most modern computers and phones making it an ideal candidate for wireless transmission. The Bluefruit LE UART is a breakout board fit with a Bluetooth low energy module and a 9600 baud rate UART [49]. If Bluetooth output is

enabled, each data point will be sent by the MCU through the TX line to the Bluetooth chip. Since the MCU is running at an internal clock frequency of 600MHz, there needs to be considerable delay between each sent point, otherwise data would be misrepresented or lost completely. A 1ms delay between each sent data point is used to prevent data loss. This delay also guarantees enough time for the Bluetooth module to send the data to any connected device before receiving the next point.

Looking at power considerations, once the module pairs with a Bluetooth friendly device, it enters connected mode which draws an average of 1.86mA. The app used to read the Bluetooth signal was created by the company that makes the Bluetooth module [51]. Powering the chip with 3.3 V from the MCU totals 6.1mW. With each digital output pin capable of up to 13.2 mW, the power consumption is less than half the maximum available power from digital output pin.

4.0 Testing Methods and Results

4.1 How to Collect the Data for Experimentation

There are two different experiments run to collect all the data presented in this thesis. The first test collected 45 HNSW samples of both steel and Sawbones. These HNSWs were taken with the transducer and an oscilloscope simultaneously to test the device's reliability and data collection methods. The second test collected an additional 100 HNSW signals collected for each material: Steel, Sawbones, PDMS and a goat cornea. PDMS and the goat cornea will be pressurized at 10mmHg, 15mmHg, 20mmHg, 25mmHg, 30mmHg. Dimensions, density, Young's modulus, and Poisson's ratio are all found in Table 1 for each discussed material.

Table 1 Geometric and mechanical properties of the samples tested in this study.

Material	Dimensions	Density (kg/m³)	Young's Modulus (GPa)	Poisson's ratio
Steel	35mm x 20mm x 28mm	7800	200	0.3
Low-Density Sawbones	35mm x 39mm x 28mm	320 [37]	0.21	0.3
PDMS	$\varnothing = 14$ mm $\times$ .6 mm	0.965 g/cm3	.360-.870 x 10^{-3}	0.5

To collect the HNSW signals from each material. The transducer is placed over top the material with the last particle of the one-dimensional chain in contact with the material's surface.

Figure 10 includes images of the transducer placement on steel, Sawbones, goat cornea, and PDMS.
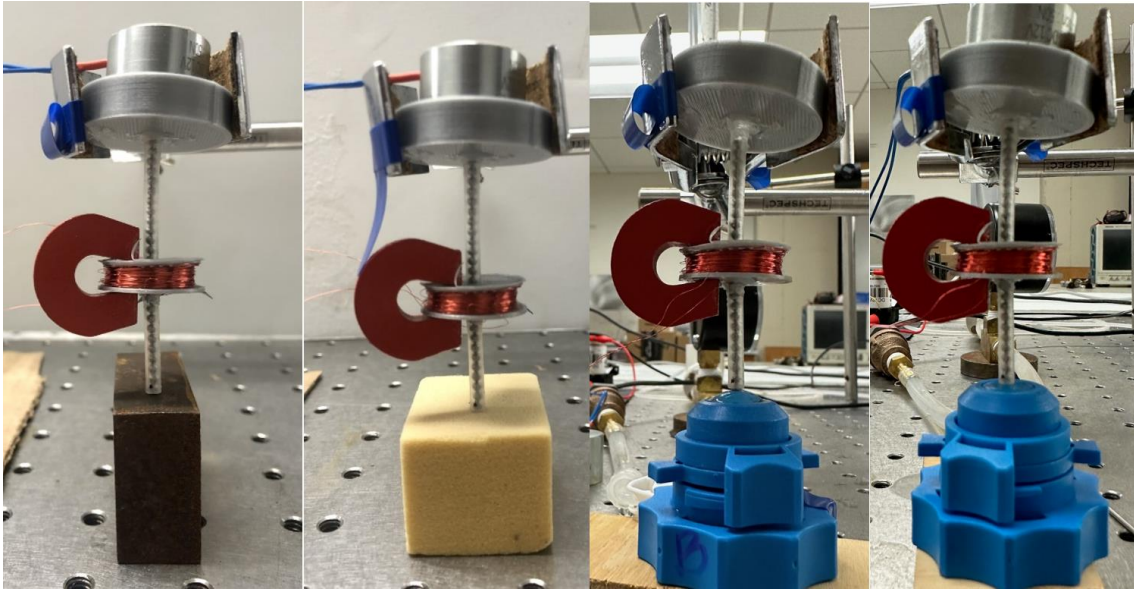
Figure 10 Transducer and its positioning over each material tested. From left to right, steel, Sawbones, goat cornea, and PDMS.

An automatic testing setup is utilized for the PDMS and goat cornea samples. The setup is typically used to mimic human (or animal) corneas and to study the biomechanics of corneas [52]. A chamber is typically used to hold cornea grafts ranging between 14 mm and 18 mm in diameter. It has two ports that allow for irrigation or aspiration of tissue while it is waiting to be implanted into a recipient's eye. For PDMS to achieve a rounded surface much like the eye, the PDMS must be fixed in place and have inward pressure pushing it into the shape. PDMS is an excellent material to replace a damaged vitreous humor through vitreoretinal surgery [52]. The testing started at 10mmHg was increased 5mmHg after 100 samples were collected until it reached 30mmHg. These values are compatible to the pressure seen in human eyes and have been represented previously in research [46, 52]. The device and a secondary microcontroller communicated to signal when the

wireless transducer was finished collecting a sample. After a predetermined number of samples was taken, the secondary microcontroller utilizes a fluid motor to fill a graduated water column until it reaches the appropriate pressure. To verify that the correct amount of water was pumped into the column, the microcontroller works in conjunction with a water pressure sensor placed on the other port of the anterior chamber holding the material. Through a feedback loop, the microcontroller polls the pressure sensor three times to assure that the system has stabilized before the next pressure value's measurements are taken. An image of the setup can be found in Figure 11.
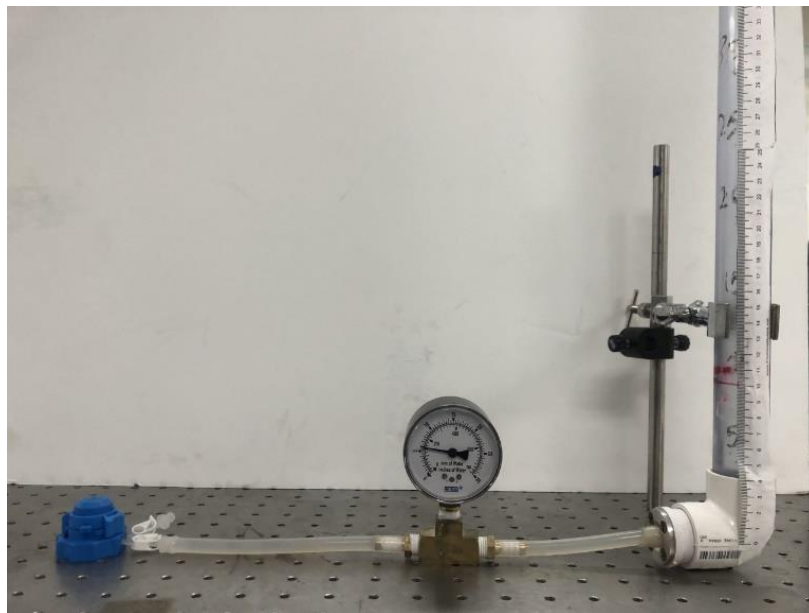
Figure 11 Setup of anterior artificial cornea chamber. The graduated cylinder is connected to one input valve and the sensor is connected to the other (not pictured).

4.2 Comparison Test of Steel and Sawbones

4.2.1 Comparison Test Methods

The purpose of this first test is to validate the hypothesis that the new wireless transducer can replace the functionality of an oscilloscope, or any other data acquisition system, that in the past was needed to collect HNSWs. The oscilloscope was set to sample the signal at 10Msps with the assumption that at this sampling rate, the entirety of the signal will be captured and can be used as a ground truth.

For data collection, the transducer was placed over either steel or Sawbones. The transducer was then connected to the device and simultaneously connected to an oscilloscope sampling at 10Msps. The oscilloscope was connected in between after the signal amplification and data conversion nodes on the device. The mean and variance of steel and Sawbones for both the device and oscilloscope are compared. A two-tailed t-test will verify whether the oscilloscope's collected HNSWs and the transducer's collected HNSW are from the same population. If they are, it verifies that the transducer and device have the functionality to adequately capture the HNSW.

In addition to the t-test, there will be a qualitative examination of overlaid signals collected from the transducer and oscilloscope to ensure that the HNSW is not excluding any other features of the wave.

4.2.2 Comparison Test Results

In each side-by-side comparison of HNSWs, the waveforms are nearly identical both in amplitude and time of arrival. The difference in ToF between the steel and the Sawbones samples are caused by the different material properties and represents one of the reasons HNSW can be used for material characterization. This is due to experimentational observation that amplitude and the ToF of the reflected wave are both functions of the stiffness of the contact material. Since the Sawbones is much softer than steel, the arrival of the reflected wave is delayed with respect to the steel sample. The results are quantified in Table 2, in terms of the ToF average and corresponding standard deviation σ, associated with the forty-five measurements.

Table 2 Results of comparative test between steel and Sawbones

Group	Count	Mean (μsec)	σ (μsec)
Steel			
Wireless Transducer	45	127	3.26
Oscilloscope	45	128	6.26
Sawbones			
Wireless Transducer	45	269	17.9
Oscilloscope	45	265	18.6

The average relative to the foam test is twice the ToF average associated with the steel sample. The standard deviation (σ) is slightly different in the oscilloscope compared to the PCB.

Likely, this is attributed to the difference in the sampling rate, which is more than 10x higher in the oscilloscope. Nonetheless, the table confirms that the wireless node is equivalent to the oscilloscope as the average values are nearly identical. The standard deviation relative to the softer material is larger. When softer materials are probed, the dynamic interaction between the solitary wave and the material gives rise to secondary effects such as material deformation and secondary pulses.

Next, the experimental mean and standard deviation values of the ToF were subjected to a two-tailed t-test to prove the ability of our device to represent the signal based on one feature and a significance of $\alpha = .05$. The compared sets have homogeneous variance, and the distribution is approximately normal. The null hypothesis was that the 90 measurements collected with the PCB and the oscilloscope on the steel sample belong to the same population and that the difference in the groups means are zero. The same hypothesis was tested for Sawbones. Both null hypotheses were rejected. The p value is 0.6835 for steel and .2789 for Sawbones, clearly indicating that all samples taken on the same material come from the same population. To further examine variabilities, the ToF associated with each measurement was placed into a 10 μsec bin (Figure 12). The graph shows that the time-waveforms associated with the steel sample were more repeatable than those associated with the Sawbones, and the oscilloscope-based and PCB-signals provided remarkably similar results. For the Sawbones sample, the ToF fell in a larger range regardless of the way the signals were collected.
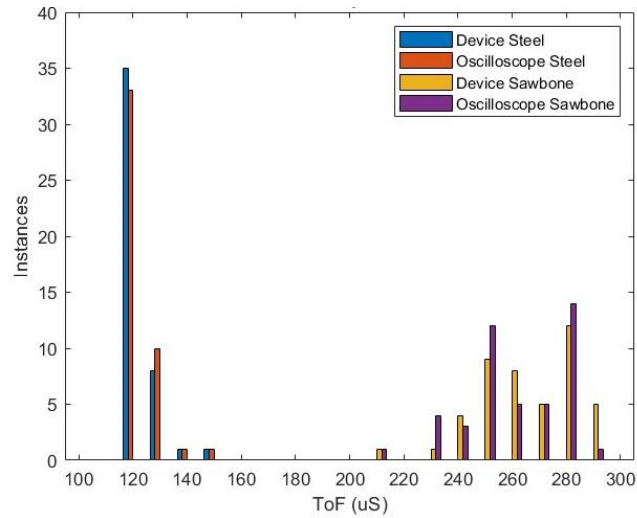
Figure 12 The ToF of steel are shown in blue and red. The ToF of Sawbone are shown in yellow and purple.

To qualitatively gauge the variability in ToFs, Figure 13 shows one waveform collected with the oscilloscope and one waveform collected with the wireless module when the transducer rested atop the steel (Figure 13A) and the polyurethane (Figure 13B) samples.
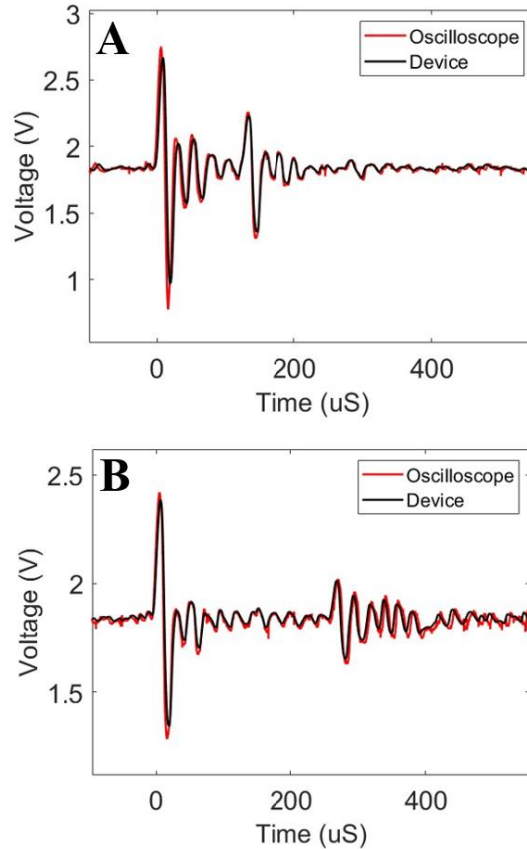
Figure 13 Typical waveforms stored with the oscilloscope and the PCB device when the array stood above (A) the steel sample and (B) the Sawbone sample.

Figure 13 presents exempliarly results where there is almost an exact overlap from the oscilloscope to the device. In another example, the formation of secondary pulses is evident in Figure 14 where the primary reflected wave is clearly tailed by at least another pulse, the SSW. It is also noted here that the ToF difference between the oscilloscope- and the PCB-based time waveform is eqaul to 13.08 μsec. In this case, the device's primary wave arrived earlier than that of the oscilloscope.

32
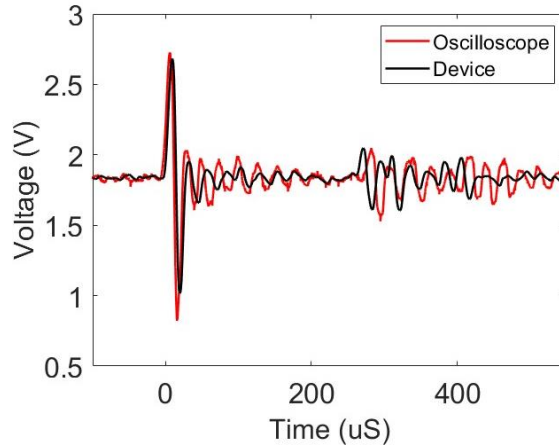
Figure 14 A case of largest differences recorded between the signals recorded with the PCB and the oscilloscope. The ToF difference is 13.08 μsec.

4.3 HNSW evaluation of all materials

One hundred measurements of HNSWs were collected for steel, Sawbones, and PDMS to gain a better understanding of their trends across materials. There are three different methods for observing the data: inspect the raw signal, pull out features unique to different materials, create a spectrogram to represent the time frequency response of the HNSW.

4.3.1 Raw HNSW Signal

One benefit to utilizing the raw signal is that there is no need for any post signal processing necessary before observing the results. This would be beneficial in realizing the final product to detect glaucoma in the eye and cut down post processing complexity. For this method,

33

each data point would be a separate feature totaling 2000 samples (around 2 mS) of captured data for one HNSW. The raw signals can be found in Figure 15.
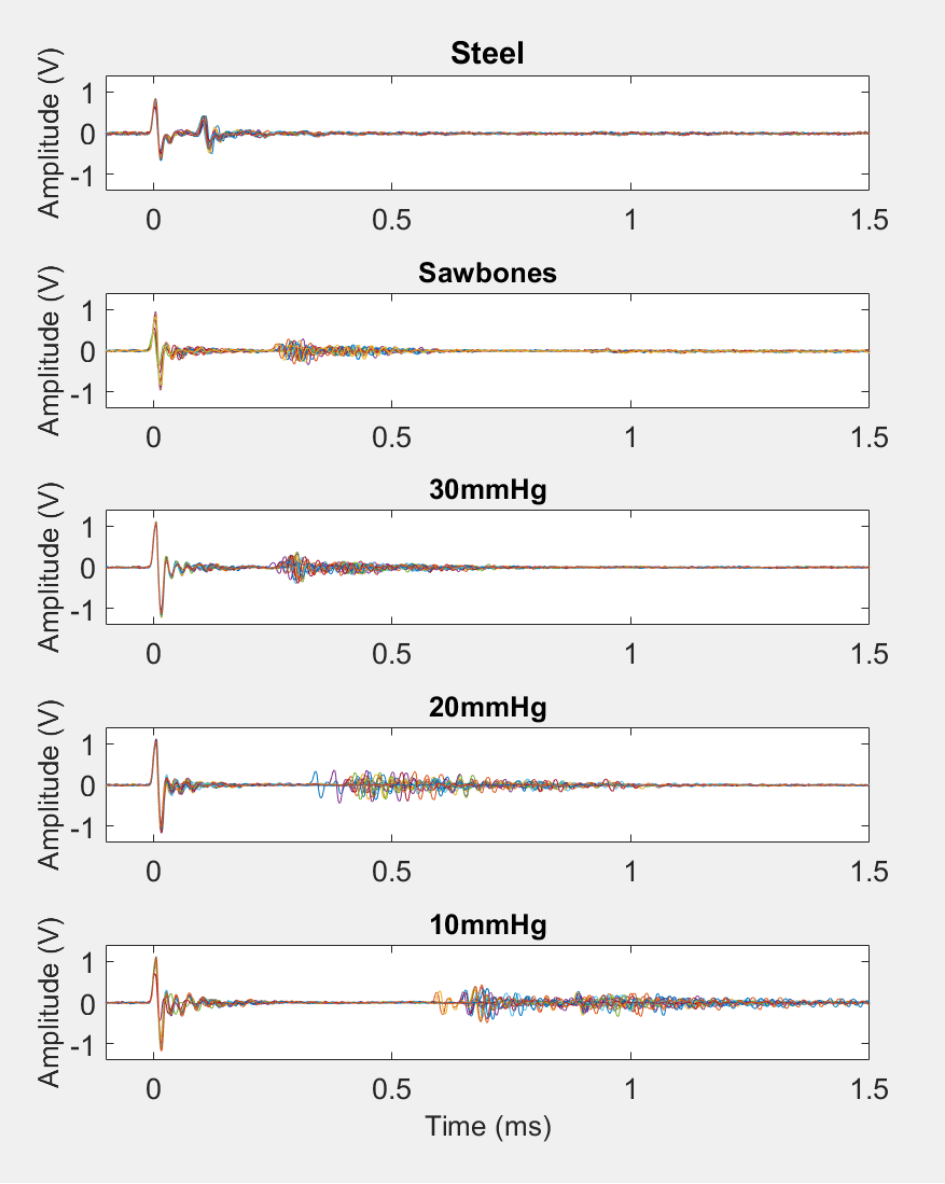
Figure 15 Raw Signals for Steel, Sawbones, and PDMS inflated between 10mmHg and 30mmHg. Only 15 samples of each HNSW are shown for simplicity.

4.3.2 HNSW Feature Vector

To cut back on the processing power needed to process the raw signal, there are 17 features extracted from each HNSW. The individual features are detailed in *Features of a HNSW*. All 17 features that represent a HNSW is considered a HNSW's feature vector. The most notable for steel, Sawbones, and PDMS—ToF for the ISW and PSW—are seen in Table 3. An error bar comparison in Figure 16 better demonstrates the ToF and its variability.

Table 3 Average and standard deviation of steel, Sawbones, and PDMS.

	Mean (μsec)	σ (μsec)
Steel	106.5	3.4
Sawbones	272.8	24.3
PDMS @ 10mmHg	680.4	108.9
PDMS @ 15mmHg	615.6	81.4
PDMS @ 20mmHg	464.9	59.3
PDMS @ 25mmHg	308.9	48.3
PDMS @ 30mmHg	275.0	20.2
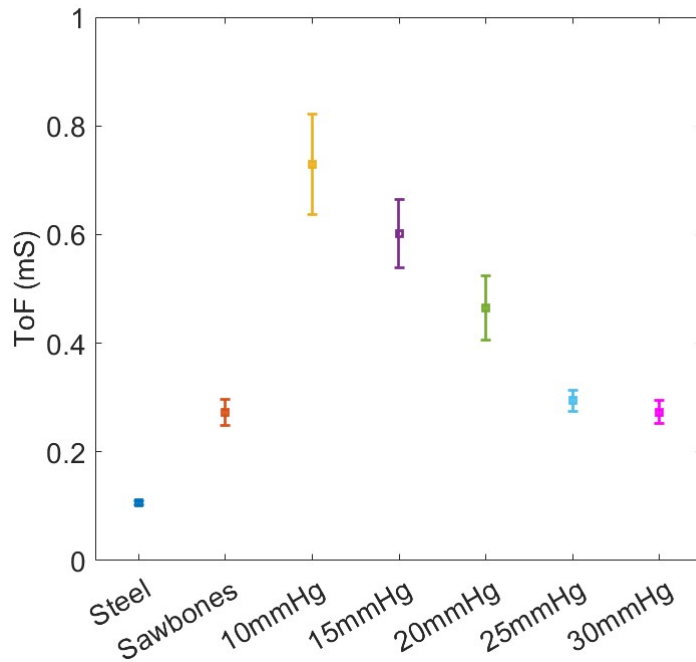
Figure 16 Error bar diagram of Steel, Sawbones, and PDMS inflated from 10-30mmHg at 5mmHg increments.

From the figure, it is evident that there is significant ToF decrease in PDMS as the pressure increase as well as a decrease in variation. Interestingly, Sawbones' ToF is similar to PDMS at 25mmHg and 30mmHg. The change in ToF is a perfect example of the difficulties when only using ToF to determine material properties. When extending to other features such as the time the PSW oscillates, it becomes more obvious of some of the differences. Sawbones has a PSW that oscillates for 269µS where PDMS at 20mmHg and 25mmHg has a PSW oscillation at 179µS and 194µS, respectively. It is believed that the higher oscillation in PDMS is due to the vibrations after contact; whereas the oscillation in Sawbones is caused by the vicinity of the PSW and SSW.

4.3.3 HNSW Spectrogram

Due to the possible issues of feature extraction overlap and raw signal noise, other methods were explored to express the HNSW. Commonly found in acoustics, spectrograms provide both valuable time and frequency components of the signal. An example of the spectrograms for PDMS can be found in Figure 17 for inflated pressures 10mmHg to 30mmHg at 5mmHg intervals. The spectrograms are created by dividing the signal into 256 sampled segments with a 220-sample overlap. A Kaiser window is used over the divided signals where $\beta = 5$.
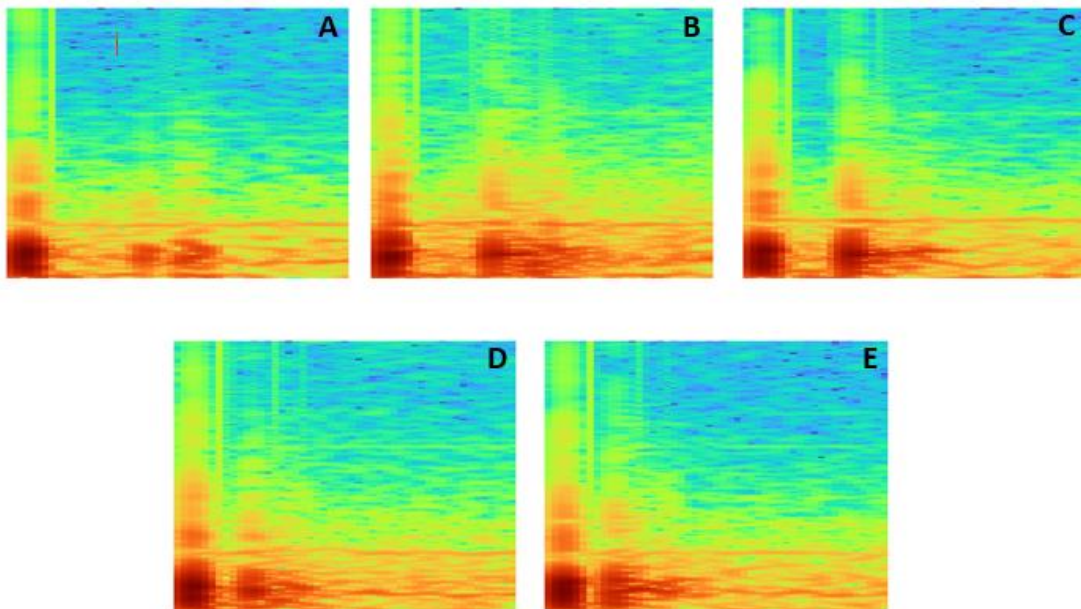
Figure 17 Spectrogram of HNSWs collected on PDMS - (A) 10mmHg, (B) 15mmHg, (C) 20mmHg , (D) 25mmHg, (E) 30mmHg.

4.4 Machine Learning Material Classification

4.4.1 Machine Learning Methods

100 HNSWs were collected for Steel, Sawbones, and PDMS to have sufficient inputs for machine learning. These inputs, the raw signal, a feature vector of the HNSW, and a spectrogram of the HNSW, will be tested for their ability to represent the material under investigation on a medium tree, SVM, subspace discriminant, narrow neural network, and CNN algorithms. Two different classification tests are run. First steel, Sawbones, and PDMS at 20mmHg followed by PDMS at 10mmHg, 15mmHg, 20mmHg, 25mmHg, and 30mmHg. The first test proves whether the HNSWs from differing materials are divergent enough to be classified with a machine learning model. The second test is designed to test the resolution of the transducer by utilizing the same material and identifying changes in its properties –pressure. PDMS is typically a material used to replace the virtuous humor in the eye and is the closest replacement for a cornea model. Therefore, the methods that were most accurate in predicting PDMS at pressures 10mmHg-30mmHg will be implemented and retrained on HNSWs collected with the designed transducer on a goat cornea at the same pressures.

4.4.2 Machine Learning Algorithms

There are 5 machine learning algorithms explored in this paper: a medium tree, linear SVM, subspace discriminant, narrow neural network, and CNN. The model hyperparameters can be found in the Appendix. Specifically, the medium tree, linear SVM, subspace discriminant, and

the narrow neural network were chosen for their performance on the first and second classification tasks.

Utilizing the MATLAB classification learner, 31 different algorithms were run on the raw signals and features [53]. The best performing algorithms are selected for a comparative analysis. The data for all classification tasks was separated into training, validation, and testing with 70%, 20%, and 10% splits, respectively. 10-fold cross-validation was utilized due to the low percentage of test data. With only 100 sample HNSWs for each material, it is important to focus the large bulk of the HNSWs to training the network. Using a 10-fold cross validation reduces the variance in the training by decreasing sensitivity to how the data is partitioned.

4.4.2.1 Medium Trees

Decision trees are a machine learning model utilizing a branching decision style for classification. At each node there is a branch that leads to another decision node. The algorithm tries to detect patterns between the classification target and the inputs. This algorithm has proven to be effective in other biological applications such as detecting inflammation of the mammary gland in cow tissue [54].

4.4.2.2 Linear SVM

Linear SVM is used in computational biology for determining splice signs in a DNA sequence [55]. Linear SVM works by separating classes of data with a linear hyperplane with a predetermined soft margin. This margin is the error above or below the hyperplane where there is crossover between classes. The soft margin is the main tunable hyperparameter found in this algorithm.

4.4.2.3 Subspace Discriminant

Subspace discriminant analysis's goal is to perform feature selection to reduce the number of inputs. For the raw signal, the subspace was reduced to 1000 inputs for the raw signal and 9 from the HNSW's extracted features. This machine learning model ranks the features by importance and assigns a 1, -1, or 0 to that feature where a 0 means that the feature provides no meaningful input towards the prediction. Like the feature extraction performed on the HNSWs, subspace discriminant has been used on extracted Mel-frequency cepstral coefficients (MFCC) from an audio signal to predict who a voice belongs to [56].

4.4.2.4 Narrow Neural Network

A neural network is modeled after the neural pathways within a brain. The algorithm utilizes interconnected nodes called neurons to send information through the model and make a prediction. Each input into a neuron has a weight which is adjusted after each iteration to decrease the cost function, typically mean squared error (MSE). In cardiovascular disease prediction, sound recordings of a patient's heart are used as inputs of various neural nets [57]. Exactly like the narrow network used in that research, the networks use one fully connected layer with a layer size of 10 and activation function ReLU.

4.4.2.5 Convolutional Neural Network

Utilizing the same structure found in a narrow neural network with interconnected neurons, the difference in a CNN is designed for computer vision. The network uses a combination of pooling and convolution layers to down-sample an image for easier classification. ECG

spectrograms have been previously used for arrhythmia classification [58]. Our CNN uses 4 convolution and pooling layers before flattening with 5 dense layers.

4.4.3 Machine Learning Results

A summary of the results can be found in Table 4 with the model's accuracy when evaluated with test data.

Table 4 Accuracy of both tests performed.

	Medium Tree	SVM	Subspace Discriminant	Narrow Neural Network	Image Classification
Material Classification Test Accuracy (%)					
Raw Signals	100	100	100	100	NA
Features	100	100	100	100	NA
Spectrogram	NA	NA	NA	NA	100
PDMS Pressure Training Test Accuracy (%)					
Raw Signals	76	83	72	80	NA
Features	76	82	76	64	NA
Spectrogram	NA	NA	NA	NA	90

From test 1, the HNSWs collected from the transducer have no issues in predicting which material is under inspection. All algorithms and inputs are accurate enough to be implemented in material classification.

To progress further towards classification of IOP, test 2 evaluates the predictive abilities of the pressurized PDMS. Here the spectrogram had the best predictive capabilities with 90% accuracy on test data. Overall, both the features and raw signals had comparable results with SVM having the second-best predictive capabilities.

Further evaluating the models, Table 5 includes the time to train each model. Classification with an image took the longest by almost 392% compared to the next highest training time. In test two there was a 422% increase in test 2.

Table 5 Training time of both tests performed.

	Medium Tree	SVM	Subspace Discriminant	Narrow Neural Network	Image Classification
Material Classification Training Time (s)					
Raw Signals	12.18	13.21	51.17	36.09	NA
Features	7.95	6.28	3.78	1.41	NA
Spectrogram	NA	NA	NA	NA	252.0
PDMS Pressure Training Time (s)					
Raw Signals	14.82	19.18	88.13	52.27	NA
Features	7.94	6.28	3.78	1.42	NA
Spectrogram	NA	NA	NA	NA	460.0

Overall, the SVM classification task with both the raw signal and features performed the best with respect to its inputs. However, the spectrogram had the highest accuracy in test 2 with

an image input. In diagnosing glaucoma, the priorities lie within accuracy rather than speed. In the same vein, the priority is accurately predicting IOP over 17mmHg rather than below that number. This is the "red flag" threshold where high IOP can start to get damaging. With these two criteria, SVM with a raw signal and feature input and a CNN with a spectrogram input can be compared to each other to identify the most fit machine learning classification algorithm for this task. An example of the input spectrograms on the goat cornea are in Figure 18.
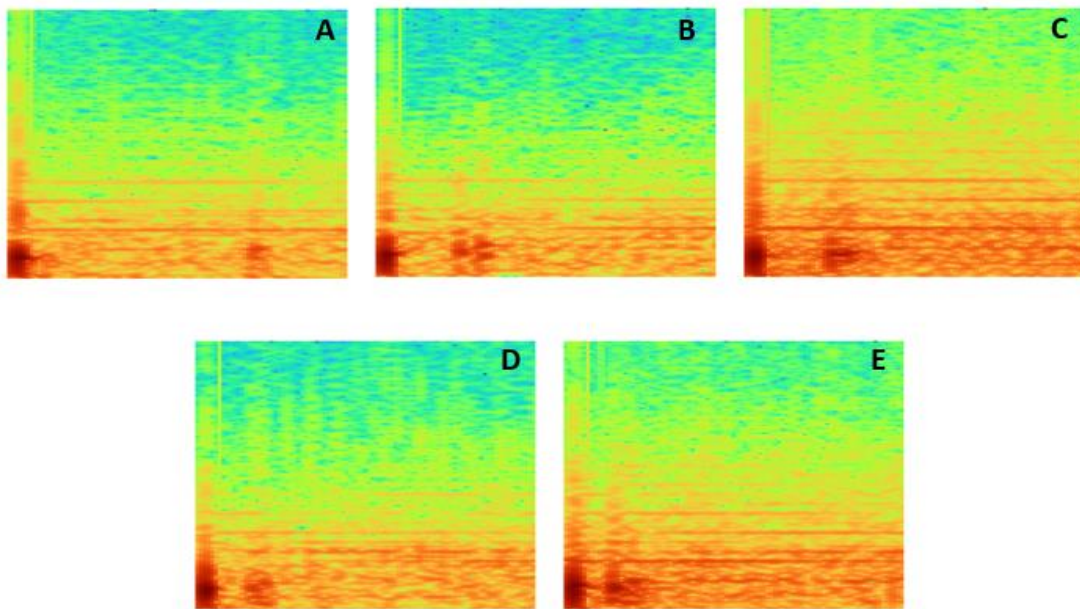
Figure 18 Spectrogram of HNSWs collected on a goat cornea - (A) 10mmHg, (B) 15mmHg, (C) 20mmHg , (D) 25mmHg, (E) 30mmHg.

The accuracy of test data and training time are presented in Table 6. The confusion matrix of the test data for the spectrograms (Figure 19A), SVM with features (Figure 19B), and SVM with the raw signal (Figure 19C) is organized by the best to worst performing.

Table 6 Accuracy and traning time for machine learning classification algorithms performed on a goat cornea.

	SVM	Image Classification
	Goat Cornea Test Accuracy (%)	
Raw Signals	50	NA
Features	72	NA
Spectrogram	NA	92
	Goat Cornea Training Time (s)	
Raw Signals	25.29	NA
Features	2.54	NA
Spectrogram	NA	569
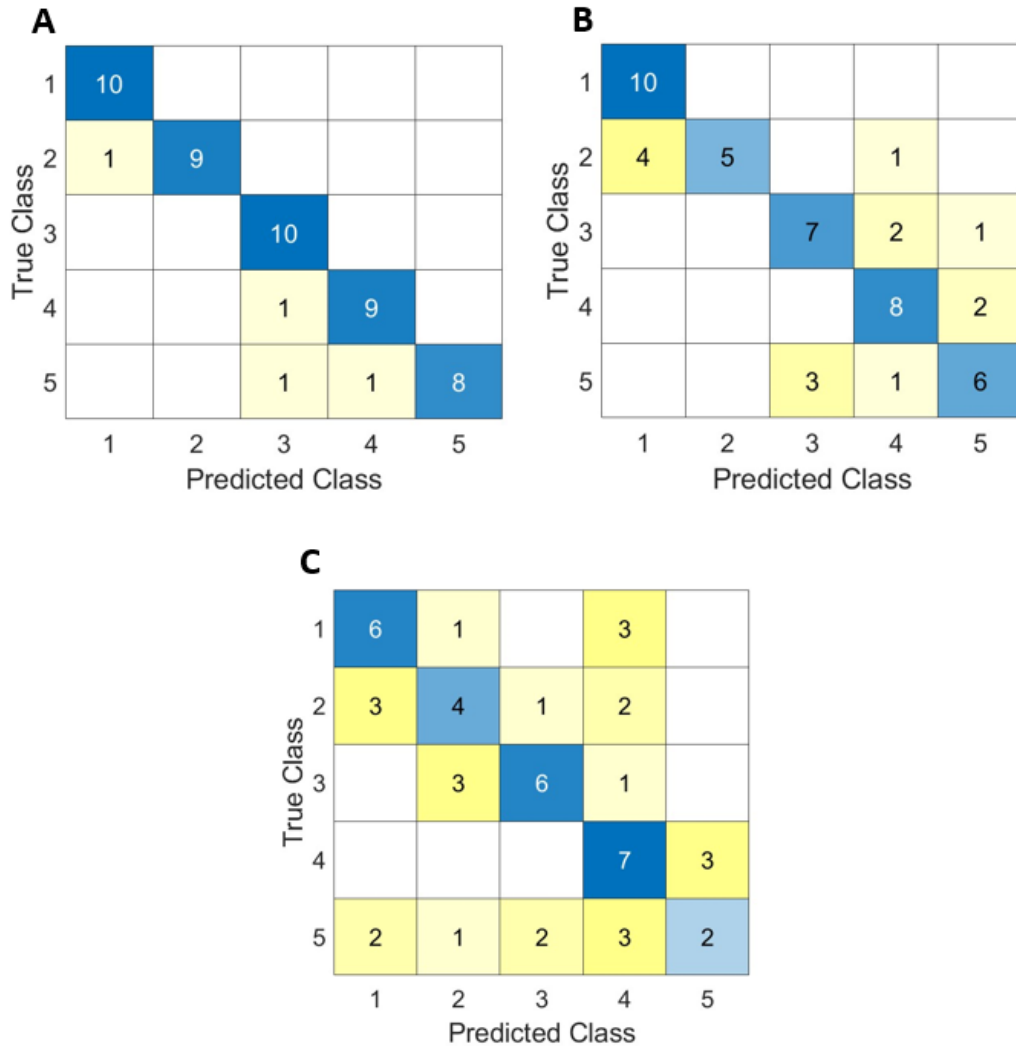
Figure 19 Confusion matrix of machine learning algorithms on test data – (A) Spectrogram with CNN, (B) Features with SVM, and (C) Raw Signal with SVM.

Looking at the results, the spectrogram is the best performing algorithm with a 20% higher accuracy on test data than the best performing SVM utilizing HNSW features. Specifically, this SVM had issues with higher IOPs. Due to the device's nature, the inability to predict high IOPs will not be enough in managing glaucoma. The spectrogram model ended with a 92% accuracy with .599 loss on test data. The train and validation accuracy for each epoch is found in Figure 20.
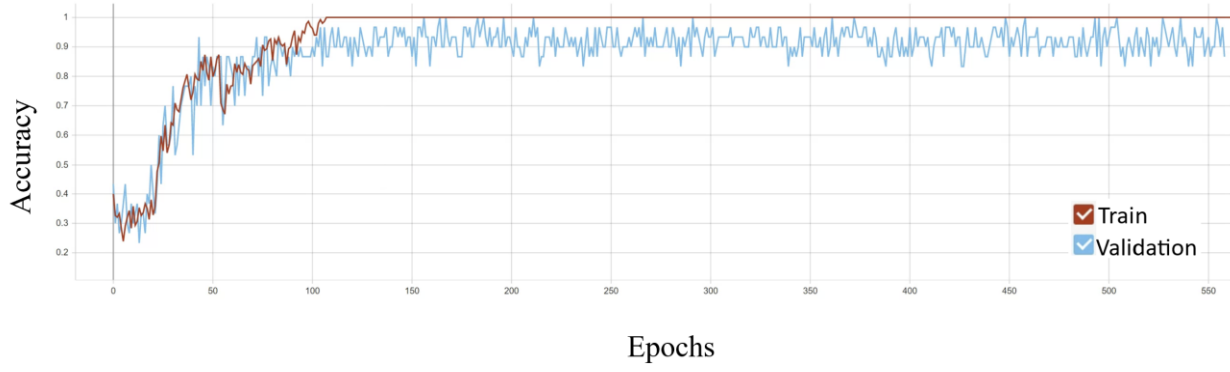
Figure 20 Train vs validation curves for the CNN testing on the goat cornea.

5.0 Conclusion

In this paper, a wireless transducer was created to collect HNSWs from differing materials to see if the HNSW is suitable for IOP classifications in a goat cornea. The transducer needed to be miniaturized from previous iterations leading to the modification of the sensing method to a coil and permanent magnet. This miniaturized transducer needed to undergo testing to evaluate its effectiveness against commonly used wired methods for sensing HNSWs. This was accomplished by comparing the side-by-side HNSWs of steel and Sawbones' on the wireless transducer and oscilloscope. By monitoring the ToF of the HNSWs, it needed to be determined whether the HNSWs came from the same population. A t-test on the 45 samples collected on steel from the device and oscilloscope and likewise with Sawbones predicted that they do indeed come from the same population with a p value of 0.6835 for steel and .2789 for Sawbones.

Now that the device was proven to be effective for measuring HNSWs, 100 additional samples were taken for steel, Sawbones, PDMS, and a goat cornea where PDMS membrane and a goat cornea were pressurized from 10mmHg-30mmHg at 5mmHg increments. The first test aimed at predicting whether the HNSWs varied enough between materials by comparing the raw HNSW signal, extracted HNSW features, and the spectrogram of steel, Sawbones, and PDMS at 20mmHg. The raw HNSW and extracted features were fed into a medium tree, linear SVM, subspace discriminant, and narrow neural network algorithms where the spectrogram was fed into a CNN. It was found that each network and input combination had a 100% accuracy on test data making all algorithms suitable for material classification.

Utilizing the same inputs and machine learning algorithms, PDMS from 10mmHg-30mmHg at 5mmHg increments was tested. The purpose of this test was to see if a similar material to a cornea would have distinguishable HNSWs for classification. It was found that the linear SVM for both raw signal and HNSW features as well as the spectrograms had the highest accuracy on test data with accuracies of 83%, 82%, and 90% respectively. Using these three instances, the goat cornea was tested which resulted in spectrograms input into a CNN being the best algorithm for IOP predictions with 92% accuracy despite its slowest training time of 569s.

6.0 Future Work

The research presented in this paper will continue by collecting more samples from corneas and measuring additional characteristics of the cornea such as the corneal thickness to increase the predictive IOP capabilities on different eyes.

After more data collection is done, there are three different directions the project can go. One of which would be modeling the characteristics of the eye to create an accurate model of HNSWs collected from an eye. Once accomplished, using this model is helpful not only in this line of research to detect IOP with a tonometer, but can be used in the greater field of ophthalmology because modelling of the human eye is extremely complex with scientific debate about the best way to model an eye.

Another direction is tuning the hyper parameters of the spectrogram and CNN as well as utilizing different machine learning algorithms to test the predictive capabilities of a HNSW. This may include testing already developed algorithms, or experimenting with different front and back ends of algorithms to develop a system that works best for this project. In addition, this direction would include exploring more features and feature combinations to increase prediction accuracy.

Finally, this project could delve deep into the circuit design aspect of the project. This includes power system management to minimize the power consumption of the device and extend battery life. Included would also be focusing on the filtering of the HNSW to minimize noise while maintaining the integrity of the signal. Improving the filtering process of the HNSW would be beneficial to other groups aimed at HNSW collection as well and encourage improvement in other HNSW transducers.

Appendix A

Table 7 Table of all features utilzied in machine learning classification task with its abbreviation, full name, and a description.

Abbreviation	Full Name	Description
ToFIP	Time of Flight Incident to Primary	Time in microseconds between the start of the ISW to the start of the PSW
ToFIS	Time of Flight Incident to Secondary	Time in microseconds between the start of the ISW to the start of the SSW
ToFPS	Time of Flight Primary to Secondary	Time in microseconds between the start of the PSW to the start of the SSW
OI	Oscillation of Incident	Time in microseconds from the start of the ISW to the end of the ISW
OP	Oscillation of Primary	Time in microseconds from the start of the PSW to the end of the PSW
OS	Oscillation of Secondary	Time in microseconds from the start of the SSW to the end of the SSW
FI	Frequency of Incident	Peak frequency content of the ISW
FP	Frequency of Primary	Peak frequency content of the PSW
FS	Frequency of Secondary	Peak frequency content of the SSW
FIA	Frequency of Incident Amplitude	Power of peak frequency content in ISW
FPA	Frequency of Primary Amplitude	Power of peak frequency content in PSW
FSA	Frequency of Secondary Amplitude	Power of peak frequency content in SSW
PE	Primary Exists	1 or 0 for the existence of a PSW
SE	Secondary Exists	1 or 0 for the existence of a SSW
RIP	Ratio of Incident to Primary	The peak-to-peak ratio of the PSW over the ISW (should be less than 1)
RIS	Ratio of Incident to Secondary	The peak-to-peak ratio of the SSW over the ISW (should be less than 1)
RPS	Ratio of Primary to secondary	The peak-to-peak ratio of the SSW over the PSW (should be less than 1)
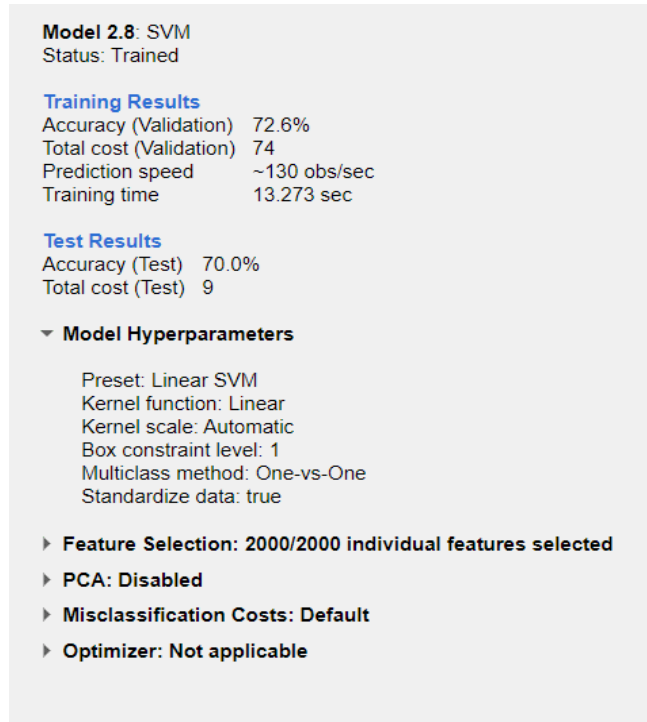
Figure 21 SVM hyperparamaters utilized in the paper.
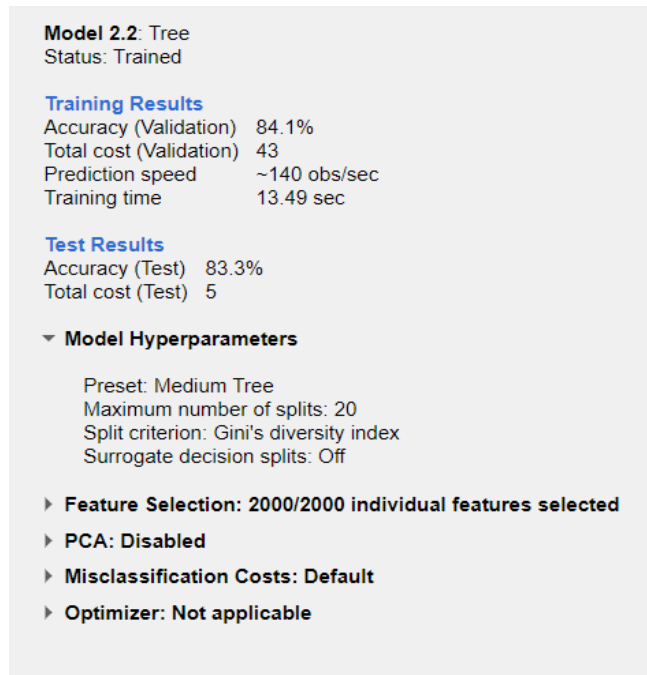
Figure 22 Medium tree hyper paramaters utlized in this paper.

Model 2.22: Ensemble
Status: Trained

Training Results
Accuracy (Validation)   66.3%
Total cost (Validation)   91
Prediction speed   ~80 obs/sec
Training time   51.53 sec

Test Results
Accuracy (Test)   46.7%
Total cost (Test)   16

▾ **Model Hyperparameters**

Preset: Subspace Discriminant
Ensemble method: Subspace
Learner type: Discriminant
Number of learners: 30

Subspace dimension: 1000

▸ **Feature Selection: 2000/2000 individual features selected**

▸ **PCA: Disabled**

▸ **Misclassification Costs: Default**

▸ **Optimizer: Not applicable**

Figure 23 Subspace discrimenant paramaters used in this paper. The subspace dimension for the raw signals was 1000 where for featutres it was 9.

Model 2.25: Neural Network
Status: Trained

Training Results
Accuracy (Validation)   74.1%
Total cost (Validation)   Not applicable
Prediction speed   ~120 obs/sec
Training time   37.283 sec

Test Results
Accuracy (Test)   76.7%
Total cost (Test)   Not applicable

▼ **Model Hyperparameters**

    Preset: Narrow Neural Network
    Number of fully connected layers: 1
    First layer size: 10
    Activation: ReLU
    Iteration limit: 1000
    Regularization strength (Lambda): 0
    Standardize data: Yes

▶ **Feature Selection: 2000/2000 individual features selected**

▶ **PCA: Disabled**

▶ **Misclassification Costs: Default**

▶ **Optimizer: Not applicable**

Figure 24 Neural network paramaters used in this paper.

Model: "sequential"

Layer (type)	Output Shape	Param #
conv2d (Conv2D)	(None, 178, 178, 16)	448
max_pooling2d (MaxPooling2D)	(None, 89, 89, 16)	0
conv2d_1 (Conv2D)	(None, 87, 87, 32)	4640
max_pooling2d_1 (MaxPooling2	(None, 43, 43, 32)	0
conv2d_2 (Conv2D)	(None, 41, 41, 64)	18496
max_pooling2d_2 (MaxPooling2	(None, 20, 20, 64)	0
conv2d_3 (Conv2D)	(None, 18, 18, 128)	73856
max_pooling2d_3 (MaxPooling2	(None, 9, 9, 128)	0
flatten (Flatten)	(None, 10368)	0
dense (Dense)	(None, 550)	5702950
dense_1 (Dense)	(None, 400)	220400
dense_2 (Dense)	(None, 300)	120300
dense_3 (Dense)	(None, 200)	60200
dense_4 (Dense)	(None, 5)	1005

Total params: 6,202,295
Trainable params: 6,202,295
Non-trainable params: 0

Figure 25 CNN hyper paramaters used in this paper. The only node that changed for each test was the final dense layer 4. This output layer changed between 3 and 5 depending on how many classification tasks were used.

Bibliography

[1] Misra, R., Jalali, H., Rizzo, P., & Dickerson, S.J. (2022). Wireless Node for Highly Nonlinear Solitary Wave Transducers. IEEE SENSORS JOURNAL, 22(4), 3540-3552.Institute of Electrical and Electronics Engineers (IEEE). doi: 10.1109/JSEN.2021.3136859.

[2] Ikegami K, Shigeyoshi Y, Masubuchi S. Circadian Regulation of IOP Rhythm by Dual Pathways of Glucocorticoids and the Sympathetic Nervous System. Invest Ophthalmol Vis Sci. 2020 Mar 9;61(3):26. doi: 10.1167/iovs.61.3.26. PMID: 32182332; PMCID: PMC7401506.

[3] Aloy MÁ, Adsuara JE, Cerdá-Durán P, Obergaulinger M, Esteve-Taboada JJ, Ferrer-Blasco T, Montés-Micó R. Estimation of the mechanical properties of the eye through the study of its vibrational modes. PLoS One. 2017 Sep 18;12(9): e0183892. doi: 10.1371/journal.pone.0183892. PMID: 28922351; PMCID: PMC5603173.

[4] R. Machiele, M. Motlagh, and B. C. Patel, "Intraocular Pressure," in StatPearls, Treasure Island (FL): StatPearls Publishing, 2022. Accessed: Feb. 13, 2022. [Online]. Available: http://www.ncbi.nlm.nih.gov/books/NBK532237/

[5] "Glaucoma Data and Statistics — National Eye Institute." https://www.nei.nih.gov/learn-about-eye-health/outreach-campaigns-andresources/eye-health-data-and-statistics/glaucoma-data-and-statistics (accessed Feb. 13, 2022).

[6] Sihota R, Angmo D, Ramaswamy D, Dada T. Simplifying "target" intraocular pressure for different stages of primary open-angle glaucoma and primary angle-closure glaucoma. Indian J Ophthalmol. 2018 Apr;66(4):495-505. doi: 10.4103/ijo.IJO_1130_17. PMID: 29582808; PMCID: PMC5892050.

[7] L. Cai, P. Rizzo, and L. Al-Nazer, "On the coupling mechanism between nonlinear solitary waves and slender beams," International Journal of Solids and Structures, vol. 50, no. 25-26, pp. 4173-4183, 2013.

[8] A. Schiffer, A. Alkhaja, J. Yang et al., "Interaction of highly nonlinear solitary waves with elastic solids containing a spherical void," International Journal of Solids and Structures, vol. 118, pp. 204-212, 2017.

[9] X. Ni, P. Rizzo, J. Yang et al., "Monitoring the hydration of cement using highly nonlinear solitary waves," NDT & E International, vol. 52, 2012.

[10] X. Ni, and P. Rizzo, "Highly nonlinear solitary waves for the inspection of adhesive joints," Experimental mechanics, vol. 52, no. 9, 2012.

[11] A. Nasrollahi, R. Lucht, and P. Rizzo, "Solitary waves to assess the internal pressure and the rubber degradation of tennis balls," Experimental Mechanics, vol. 59, no. 1, pp. 65-77, 2019.

[12] A. Nasrollahi, P. Rizzo, and M. S. Orak, "Numerical and experimental study on the dynamic interaction between highly nonlinear solitary waves and pressurized balls," Journal of Applied Mechanics, vol. 85, no. 3, 2018.

[13] Yoon, S., Kim, G., Schiffer, A., Cantwell, W. J., Kim, E., & Kim, T. Y. (2022). Detection of delaminations in AS4/PEEK composite plates using highly nonlinear solitary waves. Composite Structures, 289, 115511.

[14] Yoon, S., Cantwell, W. J., Yeun, C. Y., Cho, C. S., Byon, Y. J., & Kim, T. Y. (2023). Defect detection in composites by deep learning using solitary waves. International Journal of Mechanical Sciences, 239, 107882.

[15] Shao, Z., & Wang, Y. (2022). Study on Coupling Mechanism Between Highly Nonlinear Solitary Waves and Interior Delamination Composite Plate. Journal of Vibration Engineering & Technologies, 1-18.

[16] T.-Y.Kim, S. Yoon, C.Y. Yeun, W.J. Cantwell, C, -S. Cho,Cantwell, W. J., & Cho, C. S. (2022). Site-Specific Defect Detection in Composite Using Solitary Waves Based on Deep Learning. Lecture Notes in Civil Engineering, 2023, 270, LNCE, p442-451. B. In European Workshop on Structural Health Monitoring: EWSHM 2022-Volume 3 (Vol. 270, p. 442). Springer Nature.

[17] Jalali, H., Zeng, Y., Rizzo, P., & Bunger, A. (2021). Highly Nonlinear Solitary Waves to Estimate Orientation and Degree of Anisotropy in Rocks. Mater. Eval., 79(10).

[18] Villacreses, J. P., Caicedo, B., Caro, S. & Yépez, F. 2021. Feasibility of the use of nonlinear solitary waves for the nondestructive measurement of Young's modulus of rocks and compacted materials. Transportation Geotechnics, 26, 100437.

[19] S. Yoon, A. Schiffer, I. G. Jang et al., "Predictions of the elastic modulus of trabecular bone in the femoral head and the intertrochanter: a solitary wave-based approach," Biomechanics and Modeling in Mechanobiology, pp. 1-17, 2021.

[20] S. Yoon, A. Schiffer, J. J. Kim et al., "Numerical predictions of the interaction between highly nonlinear solitary waves and the microstructure of trabecular bone in the femoral head," Journal of the Mechanical Behavior of Biomedical Materials, vol. 109, pp. 103805, 2020.

[21] Yoon, S., Schiffer, A., Jang, I. G., Lee, S., Yeun, C. Y., & Kim, T. Y. (2022). Detection of defects in cellular solids using highly nonlinear solitary waves: a numerical study of the proximal femur. Biomechanics and Modeling in Mechanobiology, 1-14.

[22] A. Schiffer, D. Lee, E. Kim, T.-Y. Kim, "Interaction of highly nonlinear solitary waves with rigid polyurethane foams", International Journal of Solids and Structures, vol. 152–153, pp. 39-50, 2018.

[23] E. Kim, F. Restuccia, J. Yang et al., "Solitary wave-based delamination detection in composite plates using a combined granular crystal sensor and actuator," Smart Materials and Structures, vol. 24, no. 12, pp. 125004, 2015.

[24] A. Nasrollahi, and P. Rizzo, "Axial stress determination using highly nonlinear solitary waves," The Journal of the Acoustical Society of America, vol. 144, no. 4, pp. 2201-2212, 2018.

[25] A. Schiffer, R. Alia, W. J. Cantwell et al., "Elastic interaction between nonlinear solitary waves in granular chains and composite beams: Experiments and modelling," International Journal of Mechanical Sciences, vol. 170, pp. 105350, 2020.

[26] A. Schiffer, and T.-Y. Kim, "Modelling of the interaction between nonlinear solitary waves and composite beams," International Journal of Mechanical Sciences, vol. 151, pp. 181-191, 2019.

[28] T. Singhal, E. Kim, T.-Y. Kim et al., "Weak bond detection in composites using highly nonlinear solitary waves," Smart Materials and Structures, vol. 26, no. 5, pp. 055011, 2017.

[29] H. Jalali, and P. Rizzo, "Highly nonlinear solitary waves for the detection of localized corrosion," Smart Materials and Structures, vol. 29, no. 8, pp. 085051, 2020.

[30] A. Nasrollahi, and P. Rizzo, "Modeling a new dynamic approach to measure intraocular pressure with solitary waves," Journal of the mechanical behavior of biomedical materials, vol. 102, pp. 102534, 2020.

[31] S. Job, F. Melo, A. Sokolow et al., "How Hertzian solitary waves interact with boundaries in a 1D granular medium," Physical review letters, vol. 94, no. 17, pp. 178002, 2005.

[32] J. Yang, C. Silvestro, D. Khatri et al., "Interaction of highly nonlinear solitary waves with linear elastic media," Phys Rev E Stat Nonlin Soft Matter Phys, vol. 83, no. 4 Pt 2, pp. 046606, Apr, 2011.

[33] Nesterenko, V.F. (2001). Dynamics of Heterogeneous Materials, Chap.1, Springer-Verlag, NY.

[34] Daraio, C., Nesterenko, V.F., Herbold, E., and Jin, S. (2006). "Tunability of solitary wave properties in one dimensional strongly nonlinear photonic crystals." Phys. Rev. E, 73, 026610.

[35] Lazaridi A.N., and Nesterenko V.F. (1985). "Observation of a new type of solitary waves in one-dimensional granular medium." J Appl Mech Tech Phys, 26(3), 405-408.

[36] Coste C., Falcon E., and Fauve S. (1997). "Solitary waves in a chain of beads under Hertz contact." Phys Rev E, 56(5), 6104-6117.

[37] W. Deng, A. Nasrollahi, P. Rizzo et al., "On the reliability of a solitary wave based transducer to determine the characteristics of some materials," Sensors, vol. 16, no. 1, pp. 5, 2016.

[38] Luyao Cai, Piervincenzo Rizzo, Leith Al-Nazer, On the coupling mechanism between nonlinear solitary waves and slender beams, International Journal of Solids and Structures, Volume 50, Issues 25–26,2013, Pages 4173-4183, ISSN 0020 7683, https://doi.org/10.1016/j.ijsolstr.2013.08.018.

[39] Goldmann H, Schmidt T: Über Applanationstonometrie. Ophthalmologica 1957; 134:221-242. doi: 10.1159/000303213

[40] Brusini P, Salvetat ML, Zeppieri M. How to Measure Intraocular Pressure: An Updated Review of Various Tonometers. J Clin Med. 2021 Aug 27;10(17):3860. doi: 10.3390/jcm10173860. PMID: 34501306; PMCID: PMC8456330.

[41] Stevens S, Gilbert C, Astbury N. How to measure intraocular pressure: applanation tonometry. Community Eye Health. 2007 Dec;20(64):74-5. Erratum in: Community Eye Health. 2008 Jun;21(66):34. PMID: 18330450; PMCID: PMC2206330.

[42] Farhood QK. Comparative evaluation of intraocular pressure with an air-puff tonometer versus a Goldmann applanation tonometer. Clin Ophthalmol. 2013; 7:23-7. doi: 10.2147/OPTH.S38418. Epub 2012 Dec 27. PMID: 23293511; PMCID: PMC3534293.

[43] Boothe WA, Lee DA, Panek WC, Pettit TH. The Tono-Pen: A Manometric and Clinical Study. Arch Ophthalmol. 1988;106(9):1214–1217. doi:10.1001/archopht.1988.01060140374035

[44] Ruland K, Olayanju J, Borras T, Grewal DS, Fleischman D. Accuracy of Tonopen Versus iCare in Human Cadaveric Eyes With Edematous Corneas Over a Wide Range of Intraocular Pressures. J Glaucoma. 2019 May;28(5): e82-e85. doi: 10.1097/IJG.0000000000001162. PMID: 30570507; PMCID: PMC7476322.

[45] *Clear resin*. Formlabs. (n.d.). Retrieved March 24, 2023, from https://formlabs.com/store/materials/clear-resin/

[46] Pang, Y., Li, Y., Wang, X., Qi, C., Yang, Y., & Ren, T.-L. (2019). A contact lens promising for non-invasive continuous intraocular pressure monitoring. RSC Advances, 9(9), 5076–5082.

[47] R. Misra, H. Jalali, S. J. Dickerson et al., "Wireless Module for Nondestructive Testing/Structural Health Monitoring Applications Based on Solitary Waves," Sensors, vol. 20, no. 11, pp. 3016, 2020.

[48] Hodgson, M., Dickerson, S.J., Rizzo, P. (2023). Low-Power Actuation Methods for Highly Nonlinear Solitary Wave Transducers Used to Assess Human Eyes. In: Rizzo, P., Milazzo, A. (eds) European Workshop on Structural Health Monitoring. EWSHM 2022. Lecture Notes in Civil Engineering, vol 270.

[49] Industries, A. (n.d.). Adafruit bluefruit Le Uart friend - Bluetooth low energy (BLE). Adafruit industries blog RSS. Retrieved January 17, 2023, from https://www.adafruit.com/product/2479

[50] Cunningham, C. (n.d.). Bluefruit Le Connect for IOS and Android. Adafruit Learning System. Retrieved January 17, 2023, from https://learn.adafruit.com/bluefruit-le-connect

[51] Kim HJ, Seo YH, Kim BH (2017) New intraocular pressure measurement method using reflected pneumatic pressure from cornea deformed by air puff of ring-type nozzle. PLoS ONE 12(12): e0186738.

[52] Ratanapakorn T, Thongmee W, Meethongkam K, Sinawat S, Sanguansak T, Bhoomibunchoo C, Laovirojjanakul W, Yospaiboon Y. Emulsification of Different Viscosity Silicone Oil in Complicated Retinal Detachment Surgery: A Randomized Double-Blinded Clinical Trial. Clin Ophthalmol. 2020 Feb 7; 14:359-367.

[53] Regression learner. Train models to classify data using supervised machine learning - MATLAB. (n.d.). Retrieved March 24, 2023, from https://www.mathworks.com/help/stats/classificationlearner-app.html

[54] Mansour Ebrahimi, Manijeh Mohammadi-Dehcheshmeh, Esmaeil Ebrahimie, Kiro R. Petrovski, Comprehensive analysis of machine learning models for prediction of sub-clinical mastitis: Deep Learning and Gradient-Boosted Trees outperform other models, Computers in Biology and Medicine Volume 114, 2019, 103456, ISSN 0010-4825, https://doi.org/10.1016/j.compbiomed.2019.103456.

[55] Ben-Hur A, Ong CS, Sonnenburg S, Schölkopf B, Rätsch G (2008) Support Vector Machines and Kernels for Computational Biology. PLoS Comput Biol 4(10): e1000173. https://doi.org/10.1371/journal.pcbi.1000173

[56] Z. Li, W. Jiang, and H. Meng, "Fishervioce: A discriminant subspace framework for speaker recognition," 2010 IEEE International Conference on Acoustics, Speech and Signal Processing, Dallas, TX, USA, 2010, pp. 4522-4525, doi: 10.1109/ICASSP.2010.5495591.

[57] Misha Urooj Khan, Sana Samer, Mohammad Dahman Alshehri, Naveed Khan Baloch, Hareem Khan, Fawad Hussain, Sung Won Kim, Yousaf Bin Zikria, Artificial neural network based cardiovascular disease prediction using spectral features, Computers and Electrical Engineering, Volume 101, 2022, 108094, ISSN 0045-7906, https://doi.org/10.1016/j.compeleceng.2022.108094.

[58] J. Huang, B. Chen, B. Yao, and W. He, "ECG Arrhythmia Classification Using STFT-Based Spectrogram and Convolutional Neural Network," in IEEE Access, vol. 7, pp. 92871-92880, 2019, doi: 10.1109/ACCESS.2019.2928017.